Doc. S1: Supplementary materials and methods for:

The R-factor gap in macromolecular crystallography: an untapped potential for insights on accurate structures

James M. Holton[1,2], Scott Classen[2], Kenneth A. Frankel[2], John A. Tainer[3,4,5]

1. Department of Biochemistry and Biophysics, University of California, San Francisco, CA 94158-2330, USA
2. Physical Biosciences Division, Lawrence Berkeley National Laboratory, Berkeley, CA 94720, USA
3. Life Sciences Division, Lawrence Berkeley National Laboratory, Berkeley, CA 94720, USA
4. The Scripps Research Institute, La Jolla, CA, USA
5. The Skaggs Institute for Chemical Biology, La Jolla, CA, USA

Corresponding author: James M. Holton, jmholton@lbl.gov

Synopis:

Sufficient detail for reproducing the results obtained from the MLFSOM simulator program was far too extensive to fit into the printed article. Covering the breadth of literature needed to reconstruct these concepts is also a daunting task. We therefore created this document to cover this broad range of concepts in sufficient detail to satisfy and questions about not only the exact nature of our implementation of the simulator, but what decisions and compromises were made. Here we describe in detail all the physical concepts, calibrations and algorithms implemented in the MLFSOM program. This covers everything from generating structure factors from a Protein Data Bank format coordinate file, plus bulk solvent, to predicting spot positions, generating realistic X-ray background levels and detector peculiarities, spot shape, rocking curve shape and the experiments used to calibrate various sources of error that were not exhaustively explained in the main text.

Table of Contents

MLFSOM - overview

MLFSOM is dependent on the CCP4 suite (Winn, 2003), and FIT2D (Hammersley, 1997). The first stage in generating simulated diffraction images is to convert the input protein data bank (PDB) file into structure factors. This is done by the ano_sfall.com script, which decorates the molecule with hydogens using the CCP4 program HADD and calculates structure factors using SFALL. The structure factor file (mtz format) produced by this script also contains anomalous differences and a simplistic bulk solvent contribution. This or any other mtz formatted file is then submitted to the mlfsom.com script, which computes the spot positions and intensities as well as the various background contributions and noise levels and writes a FIT2D input file. These input files are fed to FIT2D which plots Gaussians and other shapes on a pixel field, applies noise and then outputs the pixel field as binary integer data. The addition of an SMV-format (Martin Stanton, SomaLogic) header enables the simulated images to be visualized and input into standard data processing programs. Detailed description of methods and assumptions for each step in calculating the simulated diffraction images is outlined here.

1. Generating structure factors

In addition to the atoms present in the PDB of interest we have also included two additional sources of contributions to the structure factors: bulk solvent and anomalous differences.

1.1. Disordered solvent contribution

In order for solvent flattening and model refinement to function normally the disordered or "bulk" solvent must be taken into account. In this work, the bulk solvent was taken from the map output by the MSKOUT feature of REFMAC. This map was normalized to have a maximum value of one, converted to structure factors using SFALL, and then the refined "partial structure" scale and B factor arrived upon in the REFMAC refinement was applied. The ano_sfall.com script will take such a phased MTZ file on its command line and add the partial structure found therein to the total structure factor before computing anomalous differences.

By default, however, ano_sfall.com will generate its own solvent mask using CAVENV or SFALL if CAVENV fails to run. This is implemented as a simple model where an electron density of 0.27 e^-/Å is assigned to each voxel in the unit cell further than 2.7 Å away from any atom in the PDB file. This is far simpler than the "true" electron density distribution in a real crystal (Lounnas *et al.*, 1994; Phillips & Montgomery Pettitt, 1995; Burling & Brünger, 1994; Makarov *et al.*, 2000), and indeed simpler than that implemented in most popular refinement packages (Tronrud, 1997; Murshudov *et al.*, 2011; Adams *et al.*, 2010). Therefore, in this case the systematic error in the bulk solvent arises because it is not sophisticated enough.

1.2. Anomalous scattering contribution

The anomalous contribution of each atom is calculated using the structure factor of atomic core electrons. This is implemented using the "Ano" atom type in the CCP4 program SFALL (Agarwal, 1978) which is equivalent in real space to constructing a single Gaussian at each atomic position with unit volume and width equivalent to the atomic B-factor. This "unit" structure factor was then converted into the anomalous and dispersive contributions of each

atom using values of f' and f" calculated by the program CROSSEC (Cromer & Waber, 1965; Waasmaier & Kirfel, 1995). The anomalous contribution of all atoms in the PDB file was accounted for, including carbon, nitrogen and oxygen. The summed anomalous signal was then added to or subtracted from the total complex structure factor of the protein and solvent to form F^+ and F^- respectively using SFTOOLS.

2. Spot Locations

The locations of diffraction spots on the detector are computed using the coordinate system and matrix formalism described in chapter 7 of (Arndt & Wonacott, 1977). The real-space unit cell with edges a, b, c and angles α,β,γ was converted into three reciprocal lattice vectors $\mathbf{a}^*$,$\mathbf{b}^*$ and $\mathbf{c}^*$ in a right-handed x-y-z coordinate system where x is the direction of the X-ray beam, z is the (horizontal) spindle axis and y is up (opposing gravity). The actual relationship between the experimental setup and gravity is, of course, irrelevant to the geometry of diffraction, but these conventions are used for convenient reference. The spindle rotation was right handed in the sense that a crystal rotation (φ) of +90º rotated a vector lying along the positive x axis onto the positive y axis. Taking the popular reference orientation where $\mathbf{a}^*$ lies perfectly along the x-axis and $\mathbf{b}^*$ lies perfectly within the x-y plane.

The x,y,z components of the three reciprocal lattice vectors were written as a 3 x 3 matrix called **B**:

$$\text{(S1)} \quad \mathbf{B} = \begin{bmatrix} a^* & 0 & 0 \\ b^*\cos\gamma^* & b^*\sin\gamma^* & 0 \\ c^*\cos\beta^* & c^*\dfrac{\cos\alpha^*\cos\beta^* - \cos\gamma^*}{\sin\gamma^*} & \dfrac{c^* V_{cell}}{a^* b^* c^* \sin\gamma^*} \end{bmatrix}$$

$a^* = bc \sin\alpha / V_{cell}$
$b^* = ca \sin\beta / V_{cell}$
$c^* = ab \sin\gamma / V_{cell}$
$\cos\alpha^* = (\cos\beta \cos\gamma - \cos\alpha)/(\sin\beta \sin\gamma)$
$\cos\beta^* = (\cos\gamma \cos\alpha - \cos\beta)/(\sin\gamma \sin\alpha)$
$\cos\gamma^* = (\cos\alpha \cos\beta - \cos\gamma)/(\sin\alpha \sin\beta)$
$V_{cell} = 2abc\sqrt{\sin(skew)\sin(skew-\alpha)\sin(skew-\beta)\sin(skew-\gamma)}$
$skew = (\alpha+\beta+\gamma)/2$

Where a* is the length of the **a*** vector, α* is the angle between **b*** and **c***, and so on. Other reference positions are possible, but this convention has been historically popular and will be used exclusively here. This **B**-matrix was then rotated using either a unitary matrix **U**, or by specifying three "missetting" angles about the x, y and z axes that generate a **U** matrix. These misseting angles were applied in the order z, y then x in keeping with the convention used in the program MOSFLM (Leslie, 2006). The product **BU** is called the **A** matrix, and represents the reciprocal lattice setting in the lab frame when the spindle position Φ is at 0. Multiplying the **A** matrix by a column vector of the Miller indices h,k,l yields the x-y-z coordinates of the corresponding reciprocal lattice point (relp), and rotating the spindle by an angle Φ will rotate the relp by the same angle about the z axis. Note that although the reciprocal unit cell angles

are not the same as the real cell angles, any rotation in real space corresponds to an identical rotation in reciprocal space. Diffraction occurs when the relp intersects the surface of the Ewald sphere, which is nominally centered at (x,y,z) = (-1/λ,0,0) and has radius 1/λ. By definition the Ewald sphere surface must intersect the origin of reciprocal space, but if the incident x-ray beam is not perfectly perpendicular to the spindle, then the center of the Ewald sphere swings away from the x-axis in the corresponding direction.

3. Spot Intensity – detector gain

We calculated the expected total number of photons in the diffracted ray of a "full" spot, just before it hits the detector, using Darwin's formula as described in the main text and in (Holton & Frankel, 2010). But this is not the intensity recorded in the final diffraction image file, the optical chain of the detector must be modeled to determine this.

The sensitivity of any x-ray detector generally changes with incident photon energy and angle of incidence. This is because the front face of most any x-ray detector consists of some kind of protective window material, followed by the x-ray sensitive layer, which itself has a finite thickness. Some of the incoming photons will be lost in the front window and not all of the photons that penetrate the window will be absorbed in the x-ray sensitive layer. The fraction of the incoming beam that is absorbed in the x-ray sensitive layer will depend on the absorption coefficient (μ) of the materials used and the incidence angle. Specifically, if the incoming beam deviates from perpendicular to the detector surface by some angle β, then the effective thickness of both the window and the x-ray sensitive layer increase by a factor 1/cosβ. Note that in the common situation where the detector plane is perpendicular to the direct beam path, β = 2θ where θ is the Bragg angle, but we will use β here for generality.

In the case of most modern CCD detectors, the window is beryllium or aluminized plastic and the x-ray sensitive layer is a finely powdered Terbium-doped Gd_2O_2S phosphor on the order of 20-40 μm thick. Once an x-ray photon is absorbed by a phosphor, a fixed fraction of its energy is converted into visible light which is emitted in all directions. This is usually about 10%, or one visible photon per 25 eV of absorbed energy (Gruner *et al.*, 1993). Some of these visible light photons are picked up by the "optical chain" of the detector, which is usually a fiber-optic bundle, and eventually a fraction of them create storable electrons in the CCD chip. The number of CCD electrons created for each incident x-ray photon is called the electro-optical gain, and ranges from 5 to 7 in current product literature. Since the initial flash of visible photons is isotropic and the losses in the optical chain are fixed, the dependence of detector sensitivity on the angle and energy of the incident x-ray photon are determined largely by the thickness of the phosphor and window. The total electro-optical gain is then given by:

$$\text{(S2)}\quad G_{eo} = \exp(-\mu_w t_w/\cos\beta)(1-\exp(-\mu_{phos} t_{phos}/\cos\beta))\cdot E_{ph}\frac{T_{bond} QE_{CCD}}{W \cdot TR^2}$$

where:

G_{eo} - electro-optical gain (CCD electrons/x-ray photon)
μ_x - absorption coefficient of window (w) or x-ray sensitive layer (phos)
t_x - thickness of window (w) or x-ray sensitive layer (phos)
β - deviation of beam from normal incidence
E_{ph} - photon energy (eV)
W - energy required to produce a visible light photon (~ 25 eV)

TR - fiber optic taper ratio (3.7)
T_{bond} - transmission of the phosphor-taper and taper-CCD bonds (~70%)
QE_{CCD} - detective quantum efficiency of the CCD (~25%)

The integer values placed in the image file ("area detector units" or ADU) are the result of amplifying and digitizing the number of electrons given by G_{eo}·photons. For ADSC products like the detector being modeled here, this amplifier gain is 3 or 4 electrons per ADU, giving ADU = photons·G_{eo}/G_{amp}. For example, consider a beam containing 100 1 Å photons impacting a typical detector (t_w = 13 μm; μ_w^{-1} = 610 μm ; t_{phos} = 40 μm; μ_{phos}^{-1} = 11 μm) at 30°. On average, 96.1 of these photons will be absorbed by the phosphor, which will generate 47,660 visible light photons. Using the bond transmission and taper ratio indicated above, only 2,437 of these will reach the CCD and produce 609 electrons of stored charge, giving a final G_{eo} of 6.1 electrons/x-ray photon and a total of 152 ADU divided over the spot if G_{amp} = 4. Although the photon losses are quite high, it is important to note that the noise is still dominated by x-ray photon counting statistics. That is, from experiment to experiment, the intrinsic variability of a spot containing an average of 100 photons will be 10% (sqrt(100) vs 100), but the variability in producing an average of 47,660 photons is only 0.46% and the variability in generating 609 electrons is 4.05%. Propagating errors[1], the total fractional noise is 10.8% or the same signal-to-noise one would get with an average of 85.7 photons incident upon a "perfect" detector, so the effective overall detective quantum efficiency (DQE) is 85.7%. For a given optical chain described by the above equation this DQE is independent of the average number of incident photons, but there are other sources of noise such as the CCD read-out noise and fractional errors in the pixel sensitivity calibration that are not taken into account by this expression of the DQE. Read noise and fractional noise will maximally affect very weak and very strong spots respectively, and this has led to some intensity-dependent definitions of the DQE, but these will not be used here. Instead, the other sources of noise will be modeled explicitly and what will be called "DQE" here is the combined effects of photon-counting noise and electron-counting noise, which is more true to the layman's concept of a DQE as the fraction of incident photons that are "detected".

Note also that there is some optimal value of β for each photon energy that maximizes G_{eo}. This is 43.7° in this example. Some additional energy dependence may arise if visible photons generated at different depths in the phosphor layer have different collection efficiencies, but this was not modeled here.

4. Spot shape

The point spread function of fiber-coupled CCD detectors was described previously (Holton *et al.*, 2012), but the transformation of an incoming beam into a spot shape is more complicated than the PSF alone. The finite depth of the detector not only influences the detected intensity, but also influences spot shape and spot position.

The shape of a diffraction spot is essentially the convolution of six processes: beam profile, beam divergence, spectral dispersion, crystal size and shape, crystal mosaic spread and detector point-spread function. However, this is not a simple convolution as it has certain geometric constraints. For example, parts of the incident x-ray beam profile that do not intersect any part of the crystal volume obviously do not contribute to diffraction spots, so the crystal extent "cuts off" the beam profile, or vice versa if the beam is smaller than the crystal. The convolution is further constrained by Bragg's Law itself, which is never violated. For

[1] $(\sigma_{total}/I_{total})^2 = (\sigma_{x\text{-}ray}/N_{x\text{-}ray})^2 + (\sigma_{vis}/N_{vis})^2 + (\sigma_{electron}/N_{electron})^2$

example, consider a Laue diffraction pattern. Although the wavelength has a broad range this will have no effect on spot shape if the mosaic spread of the crystal is zero. This is because for a given d-spacing and crystal orientation there will be one and only one sharply-defined wavelength for which the Bragg condition is satisfied. This will change if the crystal rotates, and a mosaic spread is equivalent to an isotropic rotation. This is why a finite mosaic spread leads to radial streaking of Laue spots.

If all six of the above spot-broadening processes have "zero" width, then the diffraction spot really is an incredibly sharp point, and as the crystal rotates through the Bragg condition, all of the unit cells will diffract simultaneously and instantaneously to produce a spot with the integrated energy defined by Darwin's formula. This is an important limiting case since improvements in beamline technology and crystal quality can theoretically approach zero background. As this limit is approached, radiation damage becomes the only factor limiting data quality.

However, if the "width" of one of the above parameters is not zero, then different parts of the crystal (mosaic domains) will diffract at different times, giving rise to the so-called "rocking curve" as the crystal is rotated (described below), but also giving rise to finite spot size. Both of these factors determine how much background scattering accumulates in the spot. We will now discuss each of these effects in turn starting at the detector.

4.1. Detector obliquity and parallax

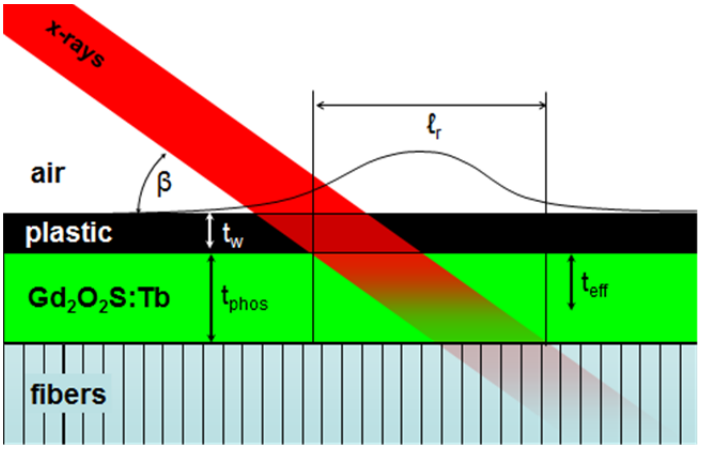

Consider a diffracted beam of width w hitting the detector plane at angle β (where β = 0 at normal incidence). At the plane of the detector surface the footprint of this beam will be w/cosβ "long" (in the radial direction) and w "wide" (In the "azimuthal" direction: normal to the beam and contained within the detector surface plane), and the increase in length 1/cosβ is called the obliquity factor. If the x-rays are strongly absorbed by the phosphor, then obliquity will define the spot shape and the centroid of the spot will be the impact point of the center of the beam. But, if the x-rays are highly penetrating and the phosphor layer is t_{phos} deep, then the beam will continue to generate light as it passes through the phosphor, and add another $t_{phos}\tan\beta$ to the radial spot size before exiting the bottom of the phosphor layer. This is called the parallax factor and both adds to the total length of the spot as well as shifts the centroid of it. Normally, the intensity of the beam falls off as it moves through the phosphor, so the effective depth is never the full t_{phos}, but some fraction of it: t_{eff}. For this calculation, t_{eff} was assigned to the depth at which half of the beam intensity had died away. The combined obliquity and parallax (OP) effect is therefore given by:

(S3.1) $\ell_r = w_r/\cos\beta + t_{eff}\tan\beta$

(S3.2) $\ell_t = w_t$

(S3.3) $t_{eff} = -2\cos\beta / \mu_{phos} \ln((1+\exp(-\mu_{phos}t_{phos}/\cos\beta))/2)$

Where:

$\ell_{r,t}$ - radial/azimuthal size of spot on detector (μm)

$w_{r,t}$ - radial/azimuthal width of diffracted beam just before hitting the detector (μm)
β - angle of incidence of the beam on the detector face (assumed in radial direction)
μ_{phos} - mass energy absorption coefficient of phosphor (μm^{-1})
t_{phos} - phosphor thickness (μm)
t_{eff} - effective phosphor thickness (μm)
Here we choose t_{eff} as twice the thickness of this same phosphor material that will yield half the light emitted by a phosphor with thickness t_{phos}. That is, half the light generated by the phosphor comes from the first $t_{eff}/2$ of depth, and the rest from the deeper layers, making t_{eff} a first-order approximation to the depth contributing to the parallax effect.

4.2. Sample size effect

Consider now the origins of w, the width of the diffracted beam just before it arrives at the detector. If the beam divergence, spectral dispersion and mosaic spread are all zero, then w will not change as the beam propagates from the crystal to the detector and the spot size will be dominated by crystal and beam size effects. That is, the diffracted beam originates in the volume of the crystal that is illuminated by the incident beam and this volume will have the width of either the incident beam or the crystal, whichever is smaller, and the same "thickness" along the direction of the incident beam as the crystal. When viewed from the detector at the spot location, this volume will still appear as wide as the beam in the azimuthal direction but elongated in the radial direction along the line between the spot location and the direct beam:

(S4.1) $w_{rx} = \ell_{box} \cos 2\theta + \ell_{xtal} \sin 2\theta$
(S4.2) $w_{tx} = \ell_{box}$

where:
w_{rx} - width of the beam in the radial direction due to the crystal/beam size
w_{tx} - width of the beam in the azimuthal direction due to the crystal/beam size
ℓ_{box} - linear size of the beam or crystal (whichever is smaller)
ℓ_{xtal} - linear depth of the crystal (along axis of incident beam)
θ - Bragg angle

In general, the radial size (but not the azimuthal size) of the resulting spot on the detector surface will be longer still due to obliquity and parallax, which was described above, but obliquity and parallax depend on detector orientation, whereas the width of the beam just before hitting the detector (w) does not. For the specific case when the detector is a flat plane perfectly normal to the incident beam, the angle β is identical to the Bragg angle 2θ, but these quantities will be kept separate here for the sake of generality.

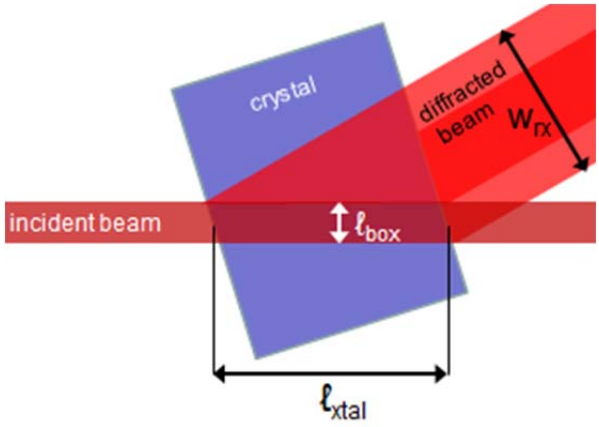

4.3. Beam divergence

Since no real x-ray beam is perfectly collimated it must spread out to some extent as it propagates through space. The rate of this spreading out can be described as an angle γ which will be called "divergence" here, but is also sometimes called "crossfire". As long as γ is a relatively small angle, the increase in beam width after the beam propagates another t meters through space will be tγ if γ is given in radians. This is the "small angle approximation".

For example, if an x-ray beam with divergence 1 milliradian passes through a 0.1 mm hole, it will be 0.1 mm wide immediately after the hole, but 1.1 mm wide one meter away from the hole. This "hole" can also be a protein crystal and the diffracted ray will "inherit" the divergence of the incident beam. That is, although the diffracted ray goes off in a different direction, the angular dispersion about that direction is the same as that of the incident beam. That is, consider a crystal with zero mosaic spread rotating in an incident beam with divergence γ. The incident beam can be thought of as a collection of zero-divergence beams that all impact the crystal at different angles. For each of these "perfect" beams, the divergence of the diffracted ray is also zero since Bragg's Law is satisfied at one and only one angle of crystal rotation, and if the crystal is stationary no more than one of these "perfect" beams will produce a diffracted ray. However, as the crystal is rotated each of the "perfect" beams will produce a diffracted ray in turn as each of them satisfies Bragg's Law, and the distribution of diffracted angles is the same as the distribution of incident angles. In fact, divergence can be thought of as equivalent to a spindle rotation in a zero-divergence beam where the detector is fixed relative to the crystal, and rotates about the crystal spindle axis during the exposure. Since divergence is generally different in the horizontal and vertical directions, they can each be thought of as a separate rotation and the effect of beam divergence on spot shape is simply to add to the existing beam width to the width induced by divergence:

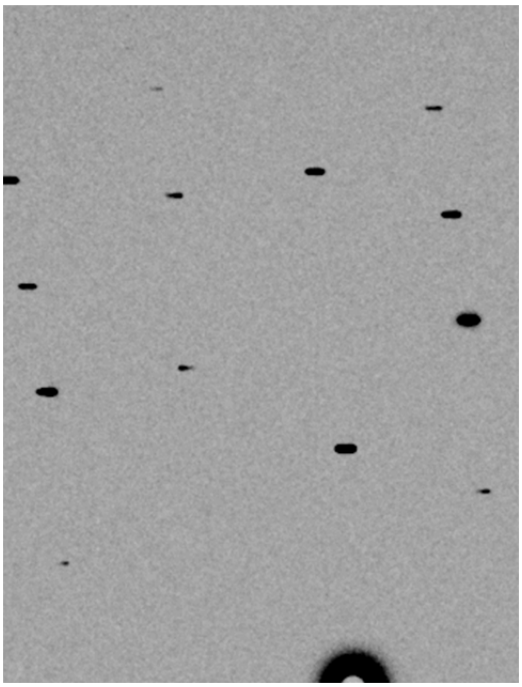

(S5.1) $w_h = t_{air}\,\gamma_h$

(S5.2) $w_v = t_{air}\,\gamma_v$

where:

w_h - width of the beam in the horizontal direction due to divergence

w_v - width of the beam in the vertical direction due to divergence

t_{air} - distance from the crystal to the spot on the detector

γ_h, γ_v - horizontal, vertical divergence, respectively (in radians)

Note that for the obliquity and parallax (OP) calculation, the angle of incidence β is not generally directed in the horizontal or vertical, so when adding the OP effects to the divergence effects the components of β in the horizontal and vertical directions must be used to calculate the OP component in the horizontal and vertical separately. A similar decomposition of β may be needed to account for OP in the radial and azimuthal directions if the detector plane is not normal to the incident beam.

4.4. Mosaic domain size – the diffraction limit

If the x-ray beam is focused on the detector, then the divergence will be negative and the spot on the detector will indeed be smaller than the crystal. But, it can never be smaller than a single mosaic block, due to the diffraction limit:

(S6) $w_{dl} = 1.22\, t_{air}\, \lambda/\ell_{mos}$

where :
w_{dl} - width of the beam in any direction due to the diffraction limit (meters)
t_{air} - distance from the crystal to the spot on the detector (meters)
λ - x-ray wavelength (meters)
ℓ_{mos} - average size of a mosaic block (meters).
If the crystal is one single mosaic domain, then ℓ_{mos} becomes ℓ_{box}, the size of the x-ray beam or the crystal, whichever is smaller. If, for example, the mosaic blocks are 10 μm and the wavelength is 1 Å detector is 82 mm away, then the minimum spot size will be 1 μm. Conversely, a 1 μm crystal will make 10 μm diffraction-limited spots.

4.5. Mosaic spread

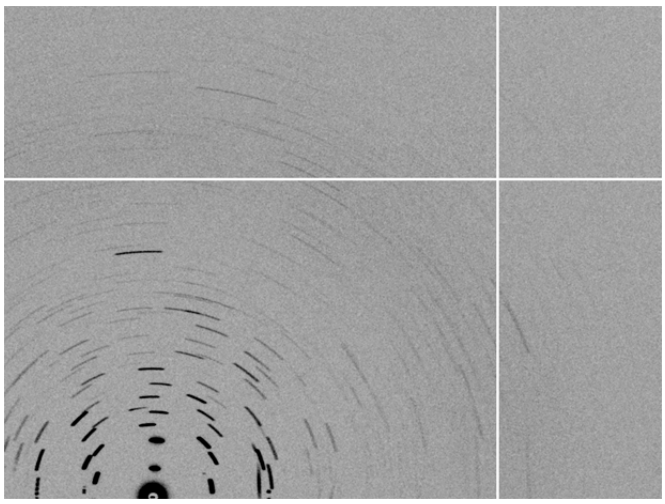

Now consider the effect of the range of different orientations of mosaic blocks (mosaic spread or "mosaicity") on spot shape. By definition, the mosaic spread is a rotation, and rotating the crystal cannot change the d-spacing of a given reciprocal lattice point (relp). That is, the relp is constrained to lie on the surface of a sphere of radius d* centered on the origin of reciprocal space. So, in the limit of "infinite" mosaic spread the diffraction spot becomes a powder ring, which is the intersection between two spheres, the Ewald sphere and the sphere of constant d*. However, mosaic spread generally refers to small rotations so the range of a particular relp due to mosaicity is a tiny patch of this sphere's surface, which is called a. Each point in the cap represents a slight rotation relative to the "average" crystal orientation, and the mosaic domains of the crystal can be represented as a collection of points bounded by the cap. This means that the mosaic spread has no effect on the radial size of the spots but only broadens the spots in the azimuthal direction. For example, as long as the beam is monochromatic, powder rings are sharp. This broadening must still satisfy Bragg's Law, so the broadening induced by a (small) mosaic spread is:

(S7) $w_{tm} = t_{air} (2\eta) 2\sin\theta$

where:
w_{tm} - width of the beam in the azimuthal direction due to mosaic spread
2η - the mosaic spread (full width of angle distribution in radians)
the factor $2\sin\theta$ arises because the mosaic rotation is about the origin of reciprocal space (amplified by the length of d*), but the diffracted ray evolves from the center of the Ewald sphere (de-amplified by the length of λ^*), and Bragg's Law dictates that the d* vector is a fraction $2\sin\theta$ of the length of λ^*. The value 2η is kept separate here because the symbol η is generally used to describe the radius of the spherical cap, but we are interested in the full width of the mosaic spread.

4.6. Spectral dispersion and unit cell variation

No x-ray beam is perfectly monochromatic, and the range of available wavelengths $\Delta\lambda$ relative to the average wavelength λ is called the spectral dispersion $\Delta\lambda/\lambda$. Dispersion has no

effect on the azimuthal spot size because changes in wavelength do not rotate the crystal, but the increase in radial spot size due to spectral dispersion can be obtained by differentiating Bragg's Law:

$\lambda = 2\, d \sin\theta$ and $\Delta\lambda/\Delta\theta = 2\, d \cos\theta \rightarrow \Delta\theta = \Delta\lambda/\lambda \tan\theta$

if θ is in radians, then the take-off angle of the spot (2θ) changes by $\Delta(2\theta) \sim 2\,\Delta\theta$ and:

(S8) $w_{rd} = t_{air}\,\Delta(2\theta) = t_{air}\,\Delta\lambda/\lambda\, 2\tan\theta$

where:
w_{rd} - width of the beam in the radial direction due to spectral dispersion
$\Delta\lambda/\lambda$ - fractional spectral dispersion (full width)
It should be noted that although mosaic spread formally cannot enlarge spots in the radial direction, any variability of unit cell dimensions will enlarge spots in the radial direction in exactly the same way as spectral dispersion:

(S9) $w_{ra} = t_{air}\,\Delta a/a\, 2\tan\theta$

where :
w_{ra} - width of the beam in the radial direction due to unit cell non-uniformity
$\Delta a/a$ - fractional variation of unit cell edge a.
Note that there is no "differential amplification" factor of λ* vs d* here as there was for mosaic spread because $\Delta\lambda/\lambda$ and $\Delta a/a$ are fractional quantities.

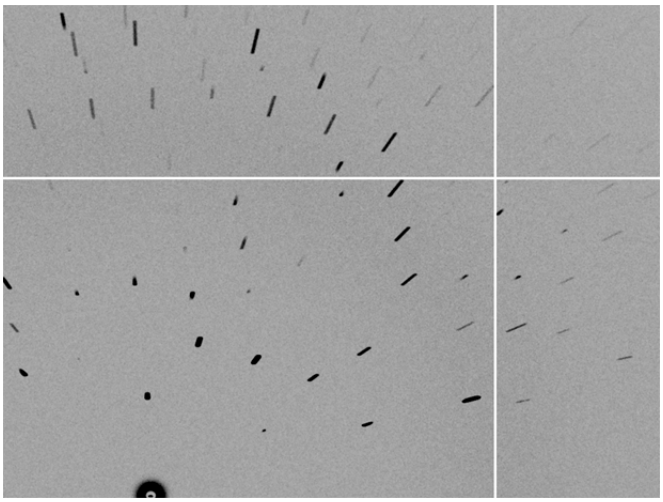

5. The rocking curve

5.1 Rocking Range

The reflecting range of each of these sub-beam and sub-crystal combinations was calculated using the equations derived by Greenhough and Helliwell (1982):

(S10.1) $$\Delta\Phi_{\eta} = (2\eta)\ \mathrm{L}\sin 2\theta$$

(S10.2) $$\Delta\Phi_{\lambda} = \Delta\lambda/\lambda\ 2\,\mathrm{L}\sin^2\theta$$

(S10.3) $$\Delta\Phi_{\gamma h} = \gamma_{\mathrm{H}}\sqrt{\left(\mathrm{L}^2\sin^2 2\theta - 1\right)}$$

(S10.4) $$\Delta\Phi_{\gamma v} = \gamma_{\mathrm{V}}$$

(S10.5) $$\Delta\Phi = L \sin 2\theta\left(2\eta + \Delta\lambda/\lambda \tan\theta\right) + \sqrt{\left(L^2 \sin^2 2\theta - 1\right)\gamma_H{}^2 + \gamma_V{}^2}$$

Where:
$\Delta\Phi_x$ - reflecting range (full range in radians) due to the effect of "x"
2η - mosaic spread (full width of rotation distribution in radians)
L - Lorentz factor
$\Delta\lambda/\lambda$ - spectral dispersion (full width)
γ_H - "horizontal" divergence along the spindle axis (full width in radians)
γ_V - vertical divergence (full width in radians)
θ - Bragg angle

All of the ranges in these equations are full widths, as opposed to half widths. Note the value 2η has been used for the full width of the crystal mosaic spread. This is because η usually appears in the literature as the radius of the spherical cap traced out by the orientations of the mosaic domains, but the full mosaic spread is of interest here. The last equation is an expression for the convolution of all these effects if they all have a "top-hat" shape, the mosaic spread is isotropic and the divergence profile has an elliptical shape. If, for example, the divergence has a rectangular shape, then in cases where the relp passes through the Ewald sphere in a corner-to-corner orientation, the true rocking range will be as much as 30% higher than that predicted by this last expression.

5.2 Shape of the rocking curve

The last section dealt with determining the "start" and "end" values of a Bragg reflection, which determines the limits of integration needed by data processing programs, but the distribution of intensity between these extremes is also important for determining accurate crystal orientation. Although often taken as the integral of a disk or sphere passing through the Ewald sphere, the exact shape of the rocking curve is more complex and indeed is different for every reflection. We shall begin as above by taking the influence of each effect in turn.

If all other parameters are negligible, the rocking curve due to a top-hat distribution of spectral dispersion or either vertical or horizontal divergence is itself a top-hat distribution. That is, the integral of spot intensity plotted against Φ is zero up until the "starting" Φ, unity at and after the "ending" Φ and forms a straight line between these two points. For example, in the case of zero mosaic spread, zero dispersion and zero horizontal divergence one can consider a finite vertical divergence to be a "fan" of evenly-spaced and zero-divergence beams impinging on the crystal. In the case of vertical divergence the "fan" has the same axis as the Φ rotation for every spot and the effect is obvious: as the crystal is rotated, each of these beams will satisfy the Bragg condition in turn, contribute an equal amount of x-rays to the spot and their influence will be evenly divided over the Φ rotation. Hence, the rocking curve has a top-hat shape. An equivalent geometric construction is to consider the relp to be an evenly-spaced series of "sub-relps" forming a line in reciprocal space centered on the "average" relp position. For a drawing, see figure 2.1 of (Arndt & Wonacott, 1977). The same model can be made of the horizontal divergence. In this case, the row of sub-relps is not aligned with the Φ rotation, but they are still evenly spaced and must pass through the Ewald sphere one at a time. The spacing between the sub-relps in terms of Φ rotation will depend on the orientation of this line in reciprocal space, but as long as the full rocking range is small enough for the

Ewald sphere surface to be considered flat, the spacing must be even and the incremental intensity per unit $\Delta\Phi$ will be a constant. A similar construction can be made for spectral dispersion: an equivalent model to constructing a range of equally-spaced Ewald spheres is to break up each relp into a radial distribution of sub-relps. These, again form an evenly-spaced line of sub-relps that pass through the Ewald sphere at a constant rate.

Since the only difference between the shape of all these top-hat rocking curves when plotted against Φ is the distance between Φ_{start} and Φ_{end}, it is convenient to normalize the progression into the rocking curve (Φ-Φ_{start}) by dividing it by $\Delta\Phi$ to yield ε. Once this is done, the plot of "partiality" p against ε is simply a line with slope equal to one:

(S11) $$p_{line}(\varepsilon) = \varepsilon$$

Where:
p_{line} - cumulative fraction of full intensity recorded
ε - (Φ-Φ_{start})/$\Delta\Phi$ normalized coordinate of rocking curve

The rocking curve due to mosaic spread, however, is not as simple since the spherical cap is a two-dimensional object in reciprocal space, but the rocking curve is still the integral of the shape of the relp as it passes through the Ewald sphere. Provided the mosaic spread is isotropic and small enough for the Ewald sphere to be considered flat, this rocking curve will be the integral of a disk:

(S12) $$p_{disk}(\varepsilon) = 2\varepsilon\sqrt{1-4\varepsilon^2} + \frac{\arcsin 2\varepsilon}{\pi} + \frac{1}{2}$$

Where:
p_{disk} - partiality of a disk-shaped relp

Note that both p and ε are normalized quantities that range from 0 to 1. Each spot will have a different $\Delta\Phi$, and this will "stretch" the rocking curve when plotted against Φ, but normalizing any mosaicity-only rocking curve using $\Delta\Phi_\eta$ from Equation (S10.1) will yield a curve that follows Equation (S10.6). However, this is only true when the divergence and dispersion are zero. If either are significant, then not only does $\Delta\Phi$ increase, but the shape of the rocking curve will lie somewhere between equations (S10.6) and (S10.7). Take for example a finite horizontal divergence and a finite mosaic spread. In this case, instead of a row of points the relp will be a stack of disks, forming an oblique cylinder in reciprocal space and the rocking curve will be the integral of this volume as it passes through the Ewald sphere. The exact shape will therefore depend on the angle made by this oblique cylinder with the Ewald sphere surface, so it is easy to see how each spot essentially has a unique rocking curve shape. Formally, the total rocking curve is the convolution of the curves arising from the mosaic spread, divergence and dispersion. If all these effects have similar $\Delta\Phi$, then the total rocking curve is reasonably approximated by that of a sphere passing through the Ewald sphere, but this assumption breaks down if one effect dominates.

6. Interactions between the rocking curve and spot shape

Combining all of these spot shape effects together requires convoluting the spot shapes that would result from each effect separately, but this convolution is complicated by spot partiality. For example, consider a horizontal beam divergence large enough to make a fully-recorded spot 10 pixels wide but we position the crystal so that the relp is equally divided between two images. On one image, only the "left" half of this 10-pixel wide spot will appear because half of the available angles in the beam did not satisfy Bragg's Law, but do on the next image, where the "right" half of the spot appears. These two spots obviously have different shapes, and similar cut-off problems exist for every combination of mosaic rotation dispersion and divergence. Furthermore, all of the above expressions for spot shape as well as the expression for the rocking width are first-order approximations and only apply for relatively small values of mosaic spread, dispersion and divergence. For example, in the absence of dispersion and divergence and mosaic spread above ~0.5° the spots start to form little arcs, and eventually turn into powder rings when the mosaic spread becomes 180°. For this simulation, these cut-off and nonlinearity problems of spot shape were solved by breaking up divergence, dispersion and mosaic spread into sub-ranges small enough for the above expressions to apply and performing the convolution for each combination of sub-ranges individually.

6.1 Gaussian kernels

The convolution of two arbitrary functions is a computationally expensive process, but the convolution of two Gaussians can be performed analytically by taking the quadrature sum of the two parent Gaussian widths. That is, since a Gaussian function has the form $\exp(-x^2)$:

(S13.1)
$$\exp\left(-\left(\frac{x}{\sqrt{w_1^{\,2}+w_2^{\,2}}}\right)^2\right) = \exp\left(-\left(\frac{x}{w_1}\right)^2\right) \otimes \exp\left(-\left(\frac{x}{w_2}\right)^2\right)$$

This is because any convolution is a product in Fourier space and the Fourier transform of a Gaussian is another Gaussian with a width that is the inverse of the width in real space. Since the width term is in the denominator of the exponent in real space, it is in the numerator in Fourier space, where the terms inside the exponent simply sum. The real space width of the convolution is therefore the square root of the sum of the squares of the two real-space Gaussian widths. For two-dimensional Gaussians with different widths in different directions, the convolution is a Gaussian whose covariance matrix is the sum of the covariance matrices of the two convoluted Gaussians:

(S13.2)
$$a = \cos^2(\theta)w_r^2+\sin^2(\theta)w_t^2$$
$$b = -\sin(2\theta)w_r^2 +\sin(2\theta)w_t^2$$
$$c = \sin^2(\theta)w_r^2+\cos^2(\theta)w_t^2$$

$$G(x,y) = \exp(-(ax^2 + bxy + cy^2))$$

$$G_1 \otimes G_2 = \exp(-((a_1+a_2)x^2 + (b_1+b_2)xy + (c_1+c_2)y^2))$$

$$w_r = ((a+c - \mathrm{sqrt}(a^2+b^2+c^2-2ac))/2)^{½}$$
$$w_t = ((a+c + \mathrm{sqrt}(a^2+b^2+c^2-2ac))/2)^{½}$$

$$\theta = \text{ArcTan}(-b/(a-c))/2$$

where subscripts denote the two Gaussians to be convoluted, w_r and w_t are the major and minor widths of a Gaussian, respectively, θ is the angle between the major axis and the x axis, and $\otimes$ is the convolution operator. Note that upon reducing to the one-dimensional case (θ=0;w_t=0), the value of w_r for the convolution reduces to the quadrature sum of w_r of the two convoluted Gaussians.

6.2 Total spot shape

The value of the above convolution algorithm in computing spot shapes lies in the fact that most any function can be approximated by a sum of Gaussians, and the convolution of a sum is the sum of the convolutions of each element of the sum. For example, a "top-hat" function (aka: "rectangular" of "boxcar" function) can be approximated by a row of evenly-spaced Gaussians that all have the same height and width. Moreover, the row of Gaussians is a very good approximation to a top-hat function convoluted with a Gaussian. For purposes of spot shape calculation all that is required is that the total idealized intensity laid down on the image be equal to the total integrated spot intensity given by Darwin's formula and that the deviations from the ideal spot shape be small when compared to photon-counting noise and the size of a pixel.

Take for example an x-ray beam divergence with a top-hat shape. If the divergence was high enough to spread a given spot over three pixels, then the incident beam was divided into three independent beams, each with one third of the flux, one third of the divergence, and with a Gaussian profile. One beam took the same direction as the original beam, and the outer two deviated by 1/3 of the divergence in either direction. This algorithm places the outer half-maximum edges of the row of Gaussians at the same position as the edges of the original top-hat, which represents the least-squares best fit of a train of three Gaussians to a top-hat function.

Continuing the example, if the spectral dispersion of the beam was large enough to spread the Bragg spots over more than one pixel, then each of the three divergence "sub-beams" was subsequently broken up into more sub-beams, each with different photon energy. In a similar way, large mosaic spreads were broken down into "sub-crystals" with different orientations. The spots produced by each combination of sub-beam and sub-crystal were then calculated using Bragg's Law, and the resulting "sub-spots" all plotted separately and summing to the total integrated intensity of the full Bragg reflection. This algorithm can lead to a combinatorial explosion of sub-spots, especially for spots that lie close to the so-called "blind region" near the rotation axis in reciprocal space. Such spots are usually rejected by integration software, so this simulation was set up to neglect spots that broke down into more than 10,000 sub-spots.

7. Background scattering

7.1 Amorphous materials

Scattering from air and other non-crystalline substances was calculated by:

$$\text{(S14)}\quad I_{bg} = \Omega_{pixel} \cdot I_{beam} \cdot t \cdot r_e^{\,2} \frac{N_A \rho \cdot V}{M_r} \cdot P \cdot A \cdot f_{bg}(s)^2$$

I_{bg} - intensity of background scattering (photons/pixel)
Ω_{pixel} - solid angle subtended by a pixel (steradians/pixel)
I_{beam} - intensity of the incident beam (photons/s/m^2)
t - exposure time (s)
r_e - classical electron radius (2.818 x 10^{-15} m/electron)
N_A - Avogadro number (6.022 x 10^{23} molecules/mol)
ρ - density of the substance (g/cm^3)
V - volume of substance exposed to the beam (cm^3)
M_r - formula weight of the substance (g/mol)
P - polarization factor
A - absorption factor
f_{bg} - structure factor of the substance (electrons)
s - reciprocal scattering vector length (sin(θ)/λ)

Note that the $N_A\rho V/M_r$ term is simply the number of molecules of the substance in the beam. For monatomic gasses, f_{bg} is the atomic structure factor, but for more complex substances such as air (a diatomic gas mixture), liquids and amorphous solids the interference between scattering from different atoms must be accounted for in f_{bg}. In general, f_{bg} is the convolution of atomic structure factors with their respective pair distribution functions, but in practice it is simplest to calibrate f_{bg} by measuring the scattering from a known quantity of the substance of interest. For this simulation, calibrated values of f_{bg} vs s for several substances such as helium, air, liquid water and Paratone-N oil were stored in text files and a simulation run specified the thickness, density, and formula weight of the substance exposed to the x-ray beam to generate a background level on an absolute scale.

For example, a 35 mm air gap between the collimator and beam-stop will scatter 434 photons/s into a low-angle 100 μm wide pixel that is 180 mm away from the sample area when the flux is 10^{12} photons/s. This is calculated using air density = 1.2 mg/cm^3, M_r ~ 28 g/mol, f_{bg} = 14 electrons (diatomic nitrogen), and Ω ~ (100 μm/180 mm)^2. Note that air scatter is independent of beam size and depends on flux only, not flux density like the scattering from a crystal. This is because the volume of illuminated air is always proportional to beam size.

7.2. Diffuse scattering

Amorphous substances are not the only thing that contributes to background scattering. An imperfect crystal will also contribute to background since the number of photons scattered by the atoms in the crystal is fixed, but the spot intensities depend on the B factor, and these "extra photons" must go somewhere. In general, the diffuse scattering from a crystal can contain information about the molecular motions that lead to excursions from a perfect lattice, but no attempt was made to simulate this here. Instead, only the first-order (centrosymmetric) term of the diffuse scattering was implemented:

$$\text{(S15)}\quad I_{ds} = \Omega_{pixel} \cdot I_{beam} \cdot t \cdot r_e^{\,2} \frac{V_{xtal}}{V_{ASU}} \cdot P \cdot A \cdot \sum_a f_a(s)^2 (1 - \exp(-2As - 2B_a s^2))$$

I_{ds} - intensity of the crystal diffuse scattering (photons/pixel)
Ω_{pixel} - solid angle subtended by a pixel (steradians)
I_{beam} - intensity of the incident beam (photons/s/m^2)

t - exposure time (s)
r_e - classical electron radius (2.818 x 10^{-15} m)
V_{xtal} - volume of the crystal (m^3)
V_{ASU} - volume of the crystal asymmetric unit (m^3)
P - polarization factor
A - absorption factor
$\sum$ - is over each atom in the asymmetric unit
f_a - structure factor of atom a (electrons)
A - is the Debye A factor derived for radiation damage above
B_a - is the Debye-Waller temperature factor of atom a ($Å^2$)
s - reciprocal scattering vector length ($\sin(\theta)/\lambda$)

Note that the diffuse scatter contributed by each atom corresponds to the background scattering that atom would produce if it were a monoatomic gas minus the photons that go into the Bragg spots, and the intensity of this diffuse scatter increases as the d-spacing decreases, making it more difficult to measure the weakening outer spots as the average B factor increases.

7.3. Compton scattering

In a similar way to the conservation of photons that leads to diffuse scattering, the finite size of the atomic form factor implies that photons scattered from electrons in the atom that do not constructively interfere must also go somewhere. This is a fairly good approximation to Compton scattering, which arises from all atoms (James, 1962). The fine structure of the inelastic scattering can contain information about the energy level structure in the substance, but no attempt was made to simulate this here. Instead, the following first-order approximation to Compton scattering was used:

(S16) $$I_{Compton} = \Omega_{pixel} \cdot I_{beam} \cdot t \cdot r_e^{\,2} \frac{V_{xtal}}{V_{ASU}} \frac{P \cdot A}{1 + \kappa (1 - \cos\theta)^2} \sum_a Z_a - \left| f_a(s) \right|$$

I_{ds} - intensity of the crystal diffuse scattering (photons/pixel)
Ω_{pixel} - solid angle subtended by a pixel (steradians)
I_{beam} - intensity of the incident beam (photons/s/m^2)
t - exposure time (s)
r_e - classical electron radius (2.818 x 10^{-15} m)
V_{xtal} - volume of the crystal (m^3)
V_{ASU} - volume of the crystal asymmetric unit (m^3)
P - polarization factor
A - absorption factor
κ - photon energy (keV) / 511 keV
$\sum$ - is over each atom in the asymmetric unit
Z - atomic number of atom a (electrons)
f_a - structure factor of atom a (electrons)
s - reciprocal scattering vector length ($\sin(\theta)/\lambda$)
Note that the structure factor term is not squared here since this is inelastic scattering and there is no constructive interference between the scattering of different electrons. This equation accounts for Compton scattering from atoms in the crystal, and not the disordered

atoms in the solvent channels and surrounding droplet. The Compton scattering from these amorphous substances is already included in the empirically calibrated value of f_{bg}, provided the wavelength of the simulation is similar to that used in the calibration.

7.4. Fluorescence

A final contributor to x-ray background is the X-ray fluorescence from heavy atoms like selenium. This was not implemented in the current version of MLFSOM.

8. Assembling everything into simulated binary image file

The main function of the mlfsom.com script is to write a very long input file for the program FIT2D. First, the vignette and calibration error masks are generated as separate fit2d-format files, which are re-used for each rendered image. The calibration error is generated by smoothing a random field of pixels and then scaling the result so the desired undulation about unity is equal to the desired RMS calibration error. After plotting a multitude of "Gaussian" peaks, which all sum up to form the spots already convoluted with the PSF, the image is multiplied by this calibration error. After this, the radially-symmetric background is added, including any specified ice rings, some small-angle scattering that is generally found around the beam stop and a direct-beam spot. A beam stop shadow may also be specified. Then photon-counting shot noise is calculated using the "POISSON" function of FIT2D. After this, a separate uniform noise field is computed for the read-out noise and added to the image along with an "ADC offset" of 40 ADU, as is conventional with images produced from ADSC detectors. Finally, a Gaussian-shaped blurring function is applied to simulate the effect of the PSF on the background pixels, the "window pane" mask between the active areas is drawn and the entire image is written out as 16-bit unsigned integers. A 512-byte text header similar to the one produced by the detector software is then prepended to this binary file. Each header contains an entry "BEAMLINE=FAKE" to help ensure that simulated images are not accidentally confused with real data.

9. Calibrating sources of error

Errors come in two flavors: random and systematic. Random errors are what "average out" when an experiment is repeated over and over, but systematic errors persist. By definition, a systematic error is a failing in the model being used to represent the system under study, either because of ignorance or because the source of error is too complicated to include in the model. Measuring systematic errors therefore requires carefully controlled experiments, which we describe below.

9.1. Photon-counting error

Deceptively simple to calculate, the square root of the number of photons sets a lower limit on the total noise in any intensity measurement, but it is important to realize that it is not the square root of the actual number of observed photons that is relevant but rather the expectation value of the average number of photons. For example, the observation of no photons does not carry with it sigma(I) = 0. Fortunately, this is not a problem for simulation, where Darwin's formula (Equation 1) gives the expectation value of the number of photons, which can be converted by the program FIT2D into a Poisson-distributed random integer.

What is a problem for the simulation is to perform this calculation on the absolute scale. For example if one beamline has a photon flux that is half that of another, but sets the detector gain to double its usual value, then the magnitude of the intensity recorded in the image file will be the same, but the error in the image will be 40% worse on the weaker source (1 vs sqrt(2)). It is also important to bear in mind that the sqrt(N) rule applies to absorbed photons only, not incident photons.

For this work, the absolute photon flux was obtained using a calibrated photodiode described by (Owen *et al.*, 2009). Some confusion has arisen over the detector gain because many data processing programs estimate it empirically by back-calculating the scale that would be required to make the RMS variation in a field of background pixels equal to the square root of the average value. This technique would work if the detector had no point-spread function (PSF), but under-estimates the gain if the pixels bleed into each other. This is because the "smoothing" effect of the PSF makes the pixels appear less noisy than the photon-counting error permits. Unfortunately, this smoothing does not reduce the error in sharp features, such as spots, so the gain estimated from the PSF-smoothed background is not appropriate to the signal in the spots. This was confirmed by simulating images where single-photon arrivals generated peaks with the shape of the PSF experimentally measured by (Holton *et al.*, 2012), with the manufacturer-specified gain of 1.8 ADU/photon. The apparent gain estimated from the RMS variation of such images was 0.6 ADU/photon, similar to that obtained for real images from this detector. For this reason, the manufacturer-specified gain was used in the MLFSOM simulation, and the smoothing effect of the PSF on the background was simulated by applying a single-Gaussian filter with FWHM = 60 um. This was found to be sufficient for suppressing the apparent detector gain to 0.6 ADU/photon and was much faster than implementing the full multi-Gaussian PSF function.

9.2. Beam flicker

No source of light is perfectly stable. In addition to the corpuscular nature of photon arrivals, which is accounted for by the "photon counting noise", there are additional variations in the "true" beam intensity over time. For example, at storage ring sources, any change in the ring current, such as top-up events, translates directly into a change in the incident intensity upon the sample. In figure S1 this "top-up noise" can be clearly seen after the "pinhole removed" time point, but with the pinhole involved other sources of noise are clearly more significant than this. The ~5% variation with an approximately 10-minute period is precisely correlated with the temperature of the cooling water for the M1 mirror (MacDowell *et al.*, 2004). The lowest point for the flux corresponds to the cooling water reaching 0.1 C above its setpoint and this triggers the compressor in the chiller to turn on. Once the setpoint is reached, the compressor turns off, and the flux, which has been rising, levels off before dropping again as the water warms up, taking about 10 minutes for each cycle. Although this variation is surprisingly large, the time scale is also very long and easily compensated for by scaling software so it does not impact data quality in any measurable way. However, the high frequency variations around this slowly-varying average flux do impact data quality. The reason why these sources of variation in beam intensity are only apparent with a pinhole inserted is because they arise not from changes in the beam position, but rather it's shape. One might think it a good idea to simply remove all pinholes, but unfortunately the crystal itself is a "pinhole" in that it is an object that intersects the beam with some cross-sectional area.

Pretty much anything that touches the x-ray beam can be a source of noise. For example, the pump that drives coolant through high power x-ray optics makes sound, as does any turbulence in the coolant flow. It is difficult to completely isolate the optics from these waves of pressure, and even very slight variations in angle are amplified by the many meters-long moment arm to the sample position. In any system where there are multiple noise sources at a variety of frequencies the total noise tends to follow a 1/f distribution where "f" is the frequency. This type of noise falls off with the square root of averaging time. That is, if averaging for 1 second at a time gives 1% error, then averaging for 0.25 seconds will give 2% error. Sampling for 0.2 seconds at a time at ALS 8.3.1 yielded 0.15% variation about the smoothly-varying thermal effect in Figure S1. Therefore, at 1 Hz 0.067% was expected, giving the "flicker noise" a value of 0.067%/sqrt(Hz). Although this was a negligible source of error for the experiment being considered here, flicker noise is expected to play an increasingly important role as detector framing rates become faster, and very high frequency flicker in the beam is perhaps an underappreciated source of beam focus size degradation.

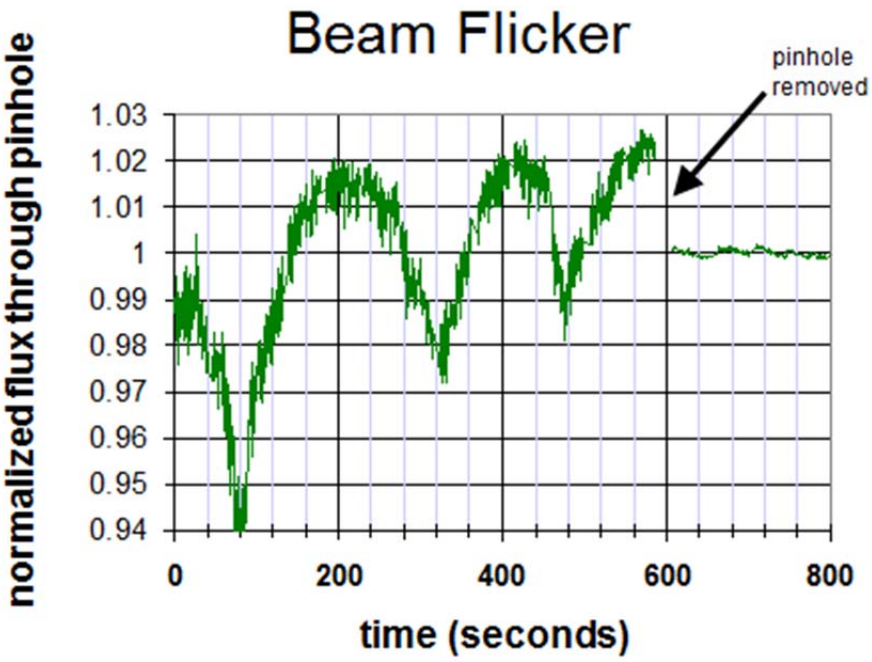

9.3. Shutter jitter

There is no such thing as "shutterless" data collection. Even for pixel arrays collecting in "shutterless" mode the per-image acquisition time is still at the mercy of the precision of electronic timing. For example, if for some reason an image file cannot be written to disk in a timely fashion, and yet the photons are still coming, what is a detector to do? One strategy is to simply keep counting and write the image when it can. This is a form of "shutter jitter".

The shutter jitter at ALS 8.3.1 was also found to be dominated by electronics, and not hardware. Specifically, the 2 millisecond "PLC" update rate of the PMAC motor controller (DeltaTau Inc., Los Angeles, CA) has a sawtooth distribution with RMS 0.577 milliseconds. By experimenting with different levels of shutter jitter in the simulation, it was found that the magnitude of the jitter was faithfully captured by the refined crystal orientation about the spindle axis. This is reported by MOSFLM as "PHIZ", and after subtracting a smooth baseline the RMS variation in PHIZ was found to be exactly sqrt(2) less than the simulated shutter jitter. That is, shutter jitter is nothing more than a change in the "true" starting and ending phi values relative to those reported in the image header. Apparently, PHIZ accurately captured the centroid of each image, which is the average of two random shutter timing errors, explaining the factor of sqrt(2). Using this rule as a guide, we analyzed the high-frequency variation in PHIZ for the real data set and found it to be RMS 0.477 ms. The similarity to the expected value of 0.408 ms, and the certainty that the PLC update rate timing error must be present

indicates that no other sources of shutter jitter were at play. If they were, the RMS PHIZ value would have been significantly higher than the PLC timing error.

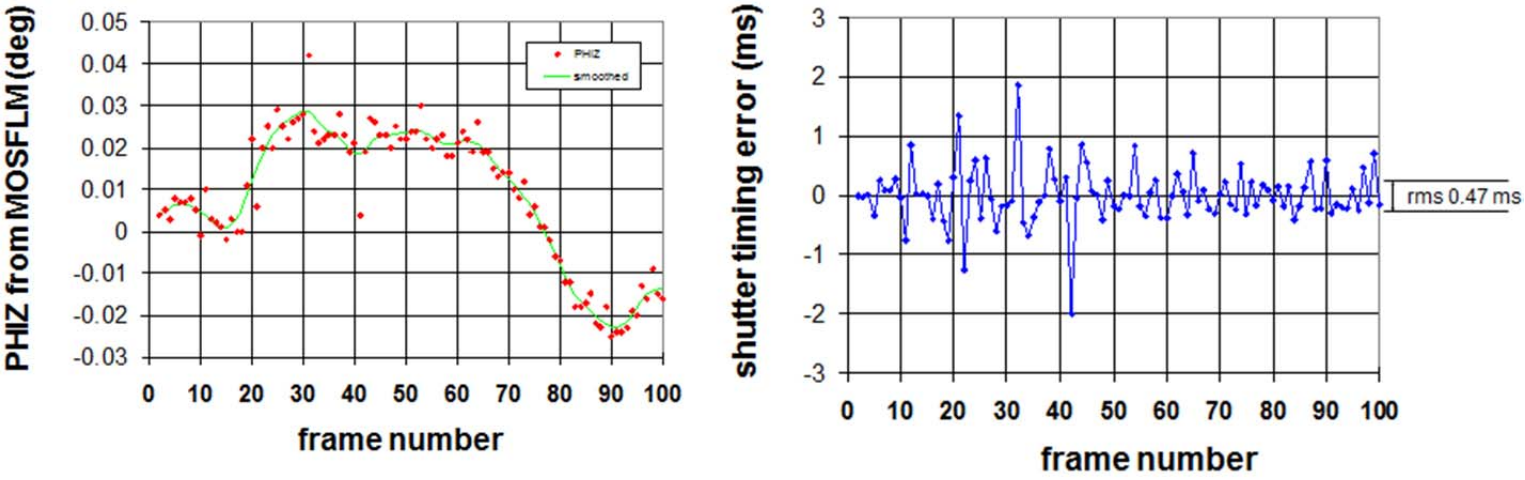

Adams, P. D., Afonine, P. V., Bunkoczi, G., Chen, V. B., Davis, I. W., Echols, N., Headd, J. J., Hung, L.-W., Kapral, G. J., Grosse-Kunstleve, R. W., McCoy, A. J., Moriarty, N. W., Oeffner, R., Read, R. J., Richardson, D. C., Richardson, J. S., Terwilliger, T. C. & Zwart, P. H. (2010). *Acta Cryst. D* **66**, 213-221.

Agarwal, R. (1978). *Acta Cryst. A* **34**, 791-809.

Arndt, U. W. & Wonacott, A. J. (1977). *The rotation method in crystallography: data collection from macromolecular crystals*. North-Holland Pub. Co., Amsterdam; New York.

Burling, F. T. & Brünger, A. T. (1994). *Isr. J. Chem.* **34**, 165-175.

Cromer, D. T. & Waber, J. T. (1965). *Acta Crystallogr.* **18**, 104-109.

Gruner, S. M., Barna, S. L., Wall, M. E., Tate, M. W. & Eikenberry, E. F. (1993). pp. 98-108.

Hammersley, A. (1997). *European Synchrotron Radiation Facility Internal Report ESRF97HA02T*.

Holton, J. M. & Frankel, K. A. (2010). *Acta Cryst. D* **66**, 393-408.

Holton, J. M., Nielsen, C. & Frankel, K. A. (2012). *J. Sync. Rad.* **19**, 1006-1011.

James, R. W. (1962). *The optical principles of the diffraction of x-rays*, repr. 1982 with addendum ed. London: Bell.

Leslie, A., G. W. (2006). *Acta Cryst. D* **62**, 48-57.

Lounnas, V., Pettitt, B. M. & Phillips Jr, G. N. (1994). *Biophys. J.* **66**, 601-614.

MacDowell, A. A., Celestre, R. S., Howells, M., McKinney, W., Krupnick, J., Cambie, D., Domning, E. E., Duarte, R. M., Kelez, N., Plate, D. W., Cork, C. W., Earnest, T. N., Dickert, J., Meigs, G., Ralston, C., Holton, J. M., Alber, T., Berger, J. M., Agard, D. A. & Padmore, H. A. (2004). *J. Synch. Rad.* **11**, 447-455.

Makarov, V. A., Andrews, B. K., Smith, P. E. & Pettitt, B. M. (2000). *Biophys. J.* **79**, 2966-2974.

Murshudov, G. N., Skubak, P., Lebedev, A. A., Pannu, N. S., Steiner, R. A., Nicholls, R. A., Winn, M. D., Long, F. & Vagin, A. A. (2011). *Acta Cryst. D* **67**, 355-367.

Owen, R. L., Holton, J. M., Schulze-Briese, C. & Garman, E. F. (2009). *J. Synch. Rad.* **16**, 143-151.

Phillips, G. N. & Montgomery Pettitt, B. (1995). *Protein Sci.* **4**, 149-158.

Tronrud, D. E. (1997). *Methods Enzymol.* **277**, 306-319.

Waasmaier, D. & Kirfel, A. (1995). *Acta Cryst. A* **51**, 416-431.

Winn, M. D. (2003). *J. Sync. Rad.* **10**, 23-25.